Full Length Article

Mapping of glacial lakes using Sentinel-1 and Sentinel-2 data and a random forest classifier: Strengths and challenges

Sonam Wangchuk [*], Tobias Bolch

Department of Geography & Sustainable Development, University of St Andrews, United Kingdom

A B S T R A C T

Glacial lakes pose a serious threat to downstream areas and significantly impact glacier melt. The number and area of lakes has grown in most regions during the last decades due to the ongoing atmospheric warming and retreating glaciers. It is therefore important to identify and monitor these lakes. However, mapping of glacial lakes in alpine regions is challenged by many factors. These factors include the small size of glacial lakes, cloud cover in optical satellite images, cast shadows from mountains and clouds, seasonal snow in satellite images, varying degrees of turbidity amongst glacial lakes, and frozen glacial lake surfaces. In our study, we have developed a fully automated method for mapping glacial lakes across alpine regions including the Python package called "GLakeMap". The method uses multi-source data such as Sentinel-1 Synthetic Aperture Radar and Sentinel-2 Multi-spectral Instrument data, a digital elevation model, and a random forest classifier model. We use multi-source datasets as inputs for rule-based segmentation of images, mainly aiming at extracting glacial lake objects from satellite images using a set of rules. Segmented objects are then classified either as glacial lake or non-glacial lake objects by the random forest classifier model. The method was tested in eight sites across alpine regions mainly located in High Mountain Asia but also in the Alps and the Andes. We show that the proposed method overcomes a majority of the aforementioned challenges to detect and delineate glacial lakes. The method performs efficiently irrespective of geographic, geologic, and climatic conditions of glacial lakes.

1. Introduction

Thousands of glacial lakes have formed in recent decades across glacierised mountain regions along with glacier retreat and global temperature rise (Pörtner et al., 2019). Some glacial lakes could be a natural water reservoir for hydropower generation and a source of water for irrigation downstream (Ehrbar et al., 2018). However, glacial lakes accelerate glacier retreat and mass loss through positive feedback mechanisms (King et al., 2019), concomitantly expanding their surface area (Komori, 2008; Wilson et al., 2018). Moreover, glacial lakes are frequently dammed by moraines and a dam failure would lead to glacial lake outburst floods (GLOFs) which pose a serious threat to downstream communities and infrastructure (Allen et al., 2019). Many glacial lakes (especially in the Himalayas) have high hazard and danger level currently, which likely will further increase in coming decades due to climate change and landscape changes around glacial lakes (Harrison et al., 2018). Hence, a detailed and up-to-date inventory and regular monitoring of glacial lakes is crucial (Emmer et al., 2016).

The definition of glacial lakes varies amongst scientific literature. For instance, for the Himalayas, glacial lakes are all the water bodies which are found above 3500 m.a.s.l (elevation) (Mool et al., 2001). Others define them as those water bodies which are located (geolocation) between the glacier terminus and the Little Ice Age moraine (Ukita et al., 2011). Moreover, glacial lakes are defined based on their hydrological connections with a glacier (Wang et al., 2015).

Broadly, these definitions are all valid as they are somehow associated with the past or present glacier activities. Different remote sensing data and techniques have been used to map glacial lakes. Glacial lakes can be manually digitised from true or false colour composites (TCC/ FCC) multi-spectral or multi-polarisation images such as acquired by Landsat (e.g. Wang et al., 2015) and Sentinel-2 or Sentinel-1 (Wangchuk et al., 2019) instrument, often aided by high-resolution images obtained from GoogleEarth or BingMaps (e.g. Zhang et al., 2015). Results from such techniques are usually accurate, but it is time-consuming when applied over a large area and is prone to inconsistencies even when delineated by experts (Rounce et al., 2017). The most commonly used semi-automated technique with optical data is the Normalised Difference Water Index (NDWI) as it enhances the presence of water bodies in

---

optical satellite imagery by using a band with relatively high reflectance of water (e.g. the blue or green band) and one with low or no reflectance (e.g. near-infrared (NIR) or short-wave infrared (SWIR) bands) (McFeeters, 1996). Frequently, slight variations in the NDWI band combinations and different NDWI thresholds are implemented depending on scenes used and study sites selected (e.g. Bolch et al., 2008; Huggel et al., 2002).

However, there are several limitations in using band indices and optical remotely sensed imagery as a whole for mapping glacial lakes. The main challenges include the small size of glacial lakes compared to large and conspicuous water bodies such as endorheic lakes on the Tibetan Plateau, cloud cover in optical satellite imagery, cast shadows from mountains, differing degrees of turbidity of glacial lakes, seasonal snows, and frozen glacial lake surfaces (Fig. 1). To map the majority of glacial lakes, the use of local thresholds derived from bimodal histograms was suggested by Li and Sheng (2012). However, removal of shadows and mapping of glacial lakes under cast shadows were still found to be problematic. Additionally, a high-turbidity glacial lake does not necessarily have a bimodal histogram as its spectral reflectance can be similar to its surrounding areas. Glacial lakes located at high elevations can remain frozen even at the end of summer and autumn seasons. A band ratio method, which uses green, SWIR and NIR bands was suggested to

map frozen glacial lakes (Wessels et al., 2002; Gardelle et al., 2011), but it is highly sensitive to glaciers. The post-processing outweighs its strength and it is not usually suitable for a large study area (Mergili et al., 2013).

The use of SAR data has been found to be robust for mapping partially frozen glacial lakes, but removal of noise around glacial lakes relies on auxiliary datasets such as glacier outlines, digital elevation model (DEM), vegetation maps derived e.g. by the Normalised Difference Vegetation Index (NDVI), and manual corrections (Wangchuk et al., 2019; Strozzi et al., 2012; Miles et al., 2017a). All these challenges stem from the fact that the spectral and radar backscatter properties of land surface in mountains are very complicated (Fig. S1). Irrespective of how advanced the existing methods are, they suffer from high commission and omission errors and requires time-consuming post-processing for large study areas. A suitable avenue and the possibility to improve accuracy of mapping land cover and many other applications is the use of machine learning techniques including a random forest classifier algorithm (e.g. Belgiu and Drăguț, 2016; Gislason et al., 2006). A random forest is made up of hundreds of individual decision trees, and the trees operate as an ensemble to produce a better class prediction than an individual tree (Breiman, 2001). Random forest has low bias and variance compared to
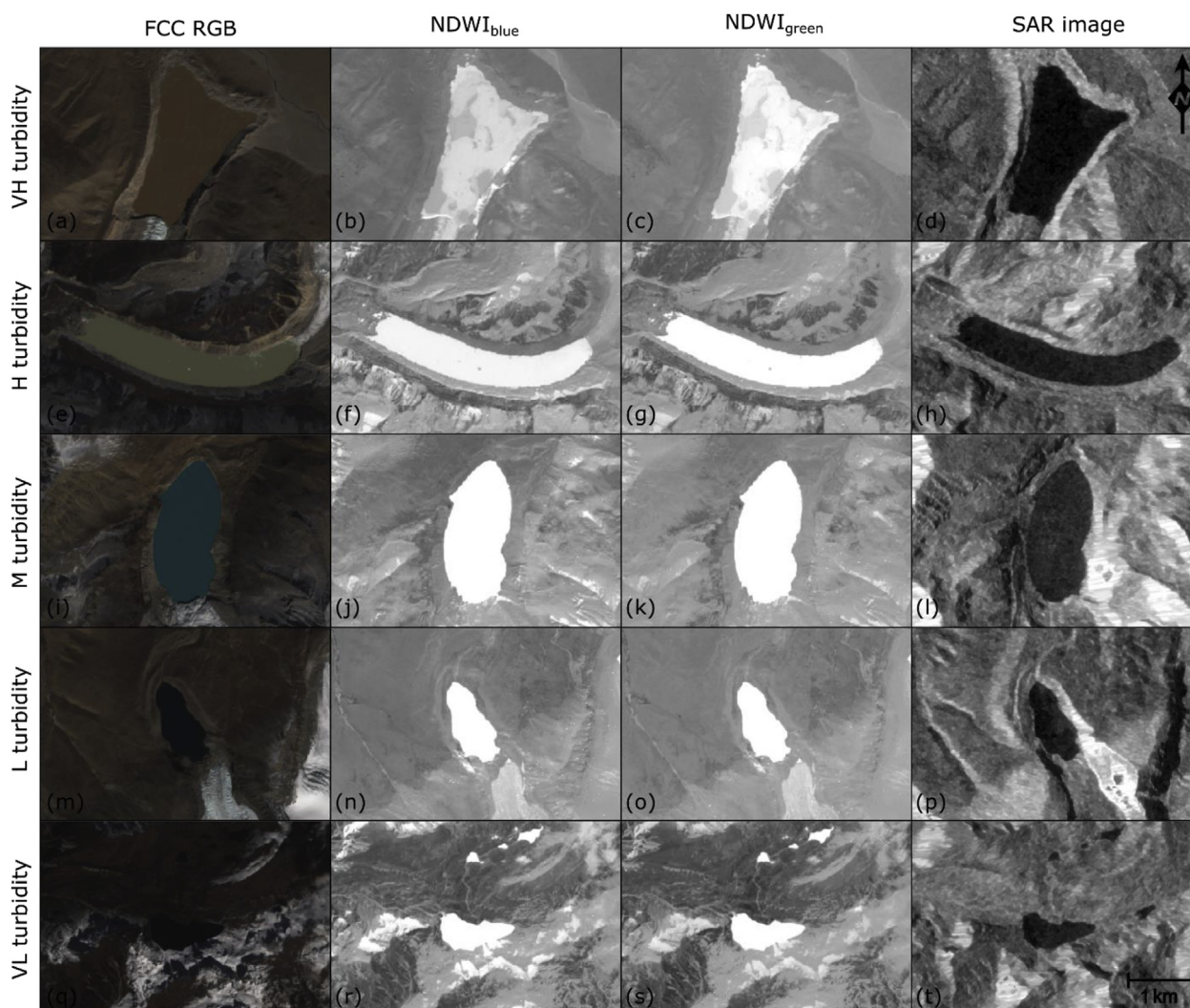
Fig. 1. Examples of varying degrees of turbidity of glacial lakes and the corresponding NDWI calculated using NIR, blue, and green bands, and sentinel-1 SAR image from the region of Bhutan Himalaya. VH: Very High (a), (b), (c) & (d); H: High (e), (f), (g) & (h); M: Medium (i), (j), (k) & (l); L: Low (m), (n), (o) & (p); LV: Very Low (q), (r), (s) & (t). NIR: near-infrared band; FCC: false colour composite; RGB: red, green, blue; NDWI: Normalised Difference Water Index; SAR: Synthetic Aperture Radar. The Sentinel-1 SAR image was acquired on 2 November 2017 and the Sentinel-2 image on 6 November 2017. (For interpretation of the references to colour in this figure legend, the reader is referred to the Web version of this article.)

an individual tree due to a random sampling of observations, a random subset of features, and binning with maximum information gain while building multiple trees and splitting nodes (Pedregosa et al., 2011). The random forest algorithm has been successfully applied in many areas of Geoscience, for instance, for mapping land cover classes (Gislason et al., 2006), detecting the past GLOF events in the Himalayas (Veh et al., 2018), and the numerous other applications (Belgiu and Drăguţ, 2016).

The purpose of this study is to develop a glacial lake mapping method and the Python package called "GLakeMap" which can map glacial lakes irrespective of cloud cover, geographic areas, climatic conditions, and glacial lake characteristics. To achieve the objective, we integrate Sentinel-1 Synthetic Aperture Radar (S-1 SAR) and Sentinel-2 Multi-spectral Instrument (S-2 MSI) data and the random forest classifier model (RFCM). The S-1 and -2 satellite images are segmented into level-0 discrete objects of interest (L-0 DOIs) using a set of rules. Then L-0 DOIs are further classified for type-I (non-glacial lake objects) and type-II DOIs (glacial lake objects) using the RFCM.

2. Test sites

We test our automated method in eight test sites across alpine regions: six sites are located in High Mountain Asia (HMA), one in the Alps, and one in the Andes. The test sites in HMA are located in the south-eastern Tibetan Plateau (Boshula mountain range), eastern Himalaya (Bhutan), central Himalaya (Koshi basin), western Himalaya (Jammu and Kashmir), central Pamir (Tajikistan), and northern Tien Shan (Kazakhstan/Kyrgyzstan) (Fig. 2). The test sites were selected to represent different topographic and climatic settings, glacial lake characteristics and hence to test the reproducibility and the accuracy of the method in different settings. The sizes of the test areas ranging between 25,000–60,000 km^2 were selected based on the availability of suitable overlapping multi-source satellite scenes (Supplemental Table S1).

The Boshula mountain range, Bhutan Himalaya, and Koshi basin are characterized by dense distribution of glacial lakes located at high elevations (Zhang et al., 2015). Glacial lakes in these regions are characterized by varying degrees of sizes, depth, and turbidity. A few glacial lakes were frozen in the satellite images we used (Supplemental Table S1). The areas remain under dense mountain shadows depending on the sun's position at the time of image acquisition by satellites. The Bhutan Himalaya and Koshi basin are influenced by the Indian monsoon, whereas the Boshula mountain range is influenced by both the Indian monsoon and the south east Asian monsoon in the summer (Yao et al., 2012); the winter is dry and cold with abundant snowfall at high altitudes (>3500 m).

Jammu and Kashmir represents the western Himalaya while the Pamir mountains are located north of the Hindu Kush Himalayas (HKH). Northern Tien Shan is located at the northern edge of HMA with overall continental climate and precipitation maxima during late spring and summer due to cyclonic activities and convection (Bolch, 2007). Glacial lakes in these regions have small sizes and could remain frozen throughout the year. They exist with mountain shadows and the turbidity varies amongst glacial lakes. The number of glacial lakes is relatively small compared to the eastern HKH (Gardelle et al., 2011). Jammu and Kashmir region is influenced by both the Indian monsoon and the westerlies, whereas the central Pamir and northern Tien Shan are dominated by the westerlies.

A majority of glacial lakes in the Swiss Alps and Peruvian Andes are not frozen in the images that were used for glacial lake mapping. The mountain shadows and turbidity of glacial lakes are similar to glacial lakes in the HKH, although the morphology and the depth of mountain shadows in images might vary. The Swiss Alps is influenced by the westerlies and Peruvian Andes by the south-easterly trade winds.

3. Data and methods

3.1. Pre-processing of datasets for rule-based image segmentation

We used Sentinel-1 Synthetic Aperture Radar (S-1 SAR) and Sentinel-2 Multi Spectral Instrument (S-2 MSI) data. These are products of the European Space Agency (ESA) and are freely available under the Copernicus program. S-1 SAR operates in C-band (5.405 GHz centre frequency) with a repeat cycle of 6 or 12 days, irrespective of day and night and weather conditions. We used level-1 ground range detected (GRD) data which has a spatial resolution of 20 by 22 m in range and azimuth directions respectively. The GRD products are focused, detected, multilooked, and projected to a ground range geometry. Additionally, we calibrated and scaled radar backscatter intensity by implementing the algorithms in the SNAP API (cf. Wangchuk et al., 2019; Peters, 2020). The S-1 SAR images were also geocoded and orthorectified using the SRTM digital elevation model (DEM) to properly align them with S-2 MSI images. The algorithms were automatically invoked and implemented using the Python module named snappy (Peters, 2020).
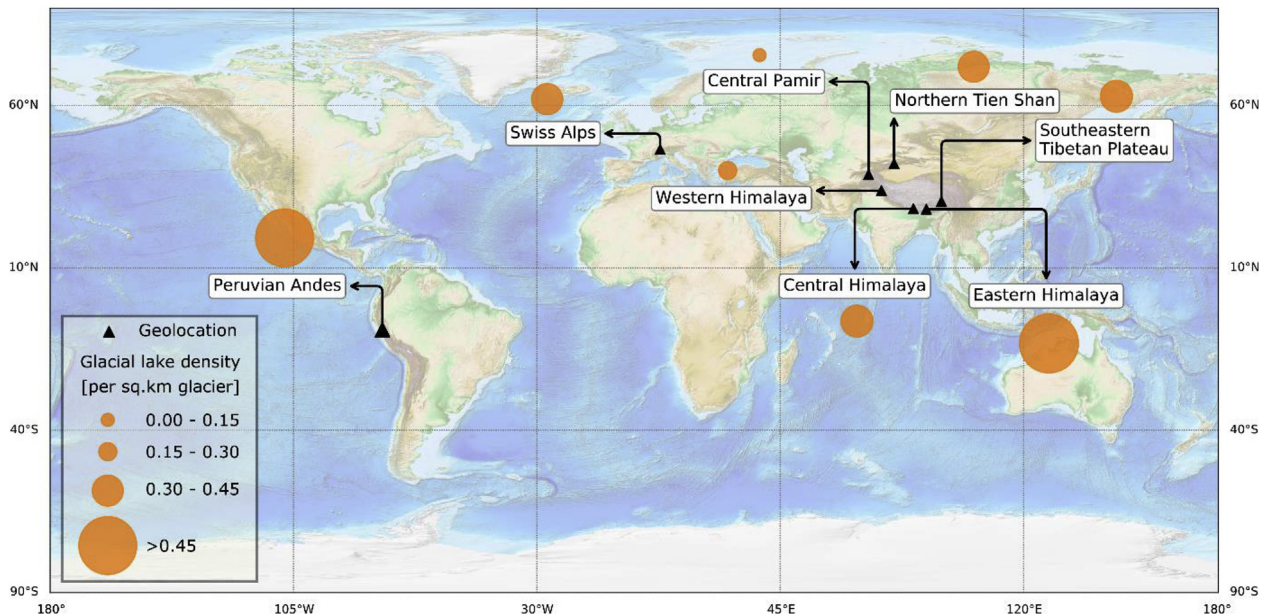

Fig. 2. Eight test sites across alpine regions of the world.

The S-2 satellites (S-2A and S–2B) have multi-spectral instruments that were designed to observe landmass and coastal areas across various wavelengths. In contrast to the S-1 SAR satellites, the S-2 MSI seonsors observe the Earth passively. The repeat cycle of each satellite is 10 days, but 5 days when both the satellites are in operation. The spatial resolution of data ranges between 10 and 60 m. We used the blue, green, and NIR bands (10 m resolution) and level-1C products as they are suitable for glacial lake mapping (Supplemental Table S1). Level-1C products are at the top of atmosphere reflectance corrected data which are freely available to users. The product of interest can be readily downloaded as tiles (each tile covers ground area of 10,000 km^2) from the Sentinel Data Hub.

The blue, green and NIR bands of S-2 MSI images were used to calculate the following NDWI:

$$NDWI_{blue} = (Blue - NIR) / (Blue + NIR) \qquad (1)$$

$$NDWI_{green} = (Green - NIR) / (Green + NIR) \qquad (2)$$

Those glacial lakes which reflect a majority of blue light are enhanced well by using equation (1) and equation (2) is suitable for glacial lakes with high green light reflectance. Therefore, we utilized strengths of both indices for enhancing alpine glacial lakes in S-2 MSI imagery. The simultaneous use of the band indices for image segmentation is possible through a use of rule-based image segmentation technique as discussed in section 3.3.

3.2. Pre-processing of predictor datasets for a random forest classifier model (RFCM)

We used six feature datasets as predictors to train a RFCM. The predictor datasets include 1) radar backscatter image, 2) NDWI$_{blue}$ image, 3) NDWI$_{green}$ image, 4) NIR image, 5) slope image, and 6) compactness ratio

(CR). The radar backscatter, NDWI$_{blue}$, and NDWI$_{green}$ images were obtained as mentioned in subsection 3.1. We also used the NIR image which has high spectral reflectance for vegetation and low reflectance for water bodies. Terrain slopes were calculated using the SRTM 30m DEM (version 3). The Neighbourhood Slope Algorithm (a.k.a average maximum technique), which is defined as the rate of maximum change in elevation between a cell and its eight neighbouring cells (Burrough et al., 1986), was used to calculate slopes and can be written as:

$$\Theta = \arctan\left(\sqrt{(\Delta x^2 + \Delta y^2)}\right) * 57.29 \qquad (3)$$

where Θ is the slope in degrees (57.29 is the conversion factor from radians to degrees), Δx is the rate of change of elevation in the x direction and Δy is the same in the y direction. The values of slope range from 0 to 90° where values close to zero represent flat surface and vice versa. The CR which measures roundness of an object was calculated as follows:

$$CR = 4\pi \frac{A}{P^2} \qquad (4)$$

where A is an area of object and P is a perimeter of the object. The values of CR range between zero and one. Those objects with rounded shape and outlines have CR values close to one, while the objects with multiple edges and jagged outlines have values close to zero. The majority of glacial lakes have CR values greater than 0.1 (Wangchuk et al., 2019).

3.3. Rule-based segmentation of satellite images

The radar backscatter, NDWI$_{green}$, and NDWI$_{blue}$ images were used as inputs to perform a rule-based image segmentation of satellite images (Fig. 3). The purpose of the rule-based image segmentation was to extract level-0 discrete objects of interest (L-0 DOIs), thus also to reduce the
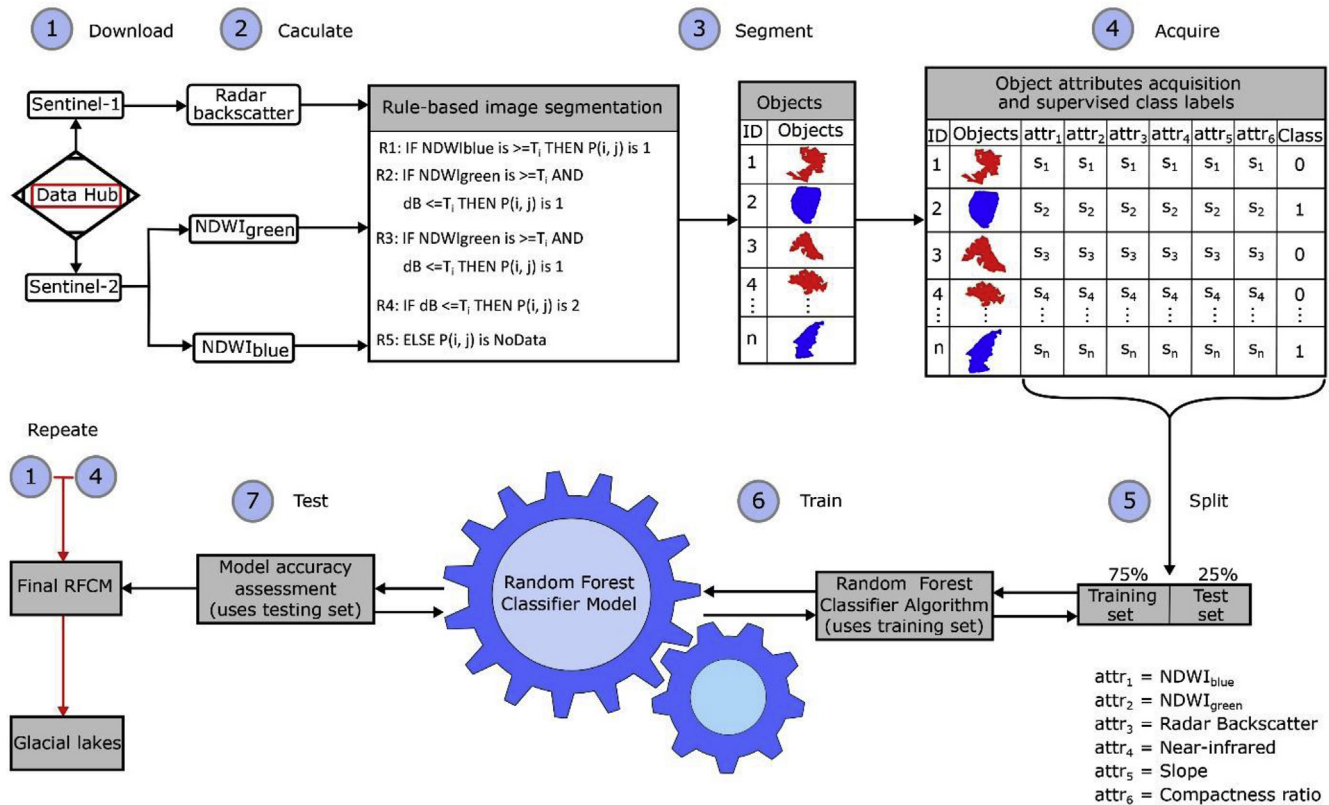

Fig. 3. Workflows for building the Random Forest Classifier Model (RFCM) (steps 1 to 7). Red objects in the diagram represent type-I DOIs with class label "0" and blue objects represent type-II DOIs with class label "1" of the L-0 DOIs. For mapping glacial lakes (making predictions on new datasets), the steps 1 to 4 are repeated except the class labelling in 4. (For interpretation of the references to colour in this figure legend, the reader is referred to the Web version of this article.)

number of non-glacial lake objects for classification. L-0 DOIs can be any objects including glacial lakes and shadows which have reflectance and radar backscatter strengths similar to open water bodies. A set of four *if − then* rules (R1, R2, R3, R4) and one *else* rule (R5) which assigned a value of 1, 2 or *No Data* to a pixel at a location *P(i,j)* was formulated using an expert system (based on the existing and expert knowledge in the field) as follows:

R1: *if* NDWI$_{blue}$ is $\geq$ T$_i$ *then* P(i,j) is 1

R2: *if* NDWI$_{green}$ is $\geq$ T$_i$ AND dB $\leq$ T$_i$ *then* P(i,j) is 1

R3: *if* NDWI$_{green}$ is $\geq$ T$_i$ AND dB $\leq$ T$_i$ *then* P(i,j) is 1

R4: *if* dB $\leq$ T$_i$ *then* P(i,j) is 2

R5: *else* P(i,j) is *No Data*

where T$_i$ were manually defined thresholds for S-2 NDWI images and S-1 radar backscatter image. The first three rules assigned a value of 1 and the fourth and fifth rules assigned a value of 2 and *No Data* respectively to a pixel at a particular location *P(i,j)*. The R1 rule was designed to extract L-0 DOIs having NDWI$_{blue}$ values greater than or equal to 0.6, representing mostly low-turbidity glacial lake objects. The R2 and R3 rules with NDWI$_{green}$ thresholds 0.05 and 0.30 were used to extract L-0 DOIs with medium- and high-turbidity. The R4 rule which used only S-1 radar backscatter image and a threshold value of −14 dB was designed to segment L-0 DOIs when optical data are obscured by partial or full cloud cover. It is important to note here that pixels were assigned a value of 2 to avoid aggregation with the pixels that satisfied the former rules and to distinguish from other pixels. All input pixels must be evaluated (a pixel has to satisfy one of the functions to be selected as glacial lake pixels) using the relevant thresholds to yield a single scalar output.

3.4. Training random forest classifier model

To train the Random Forest Classifier Model (RFCM), 1790 L-0 DOIs samples were collected from the test sites located in eastern Himalaya, central Himalaya, and south-eastern Tibetan Plateau. They were used as zones (regions) to calculate the average value of each predictor (six predictors in total: radar backscatter, NDWI$_{blue}$, NDWI$_{green}$, NIR, slope, CR) within their zones. Furthermore, the samples were divided into non-glacial lake objects which we call type-I DOIs and glacial lake objects which we call type-II DOIs hereafter. The sample observations that belong to type-I DOIs (e.g. red objects in Fig. 3) were labelled "0" and labelled "1" for type-II DOIs (e.g. blue objects in Fig. 3) to a create target class of the RFCM. The labelling of type-I and type-II DOIs was aided by S-2 TCC/FCC images, high resolution Google Earth images, and existing glacial lake inventory datasets where reference datasets are available (e.g. Ukita et al., 2011; Zhang et al., 2015). The labelled samples were then split into a training set and a testing set. The training set was composed of 75% (1342) of samples, whereas the testing set was composed of 25% (448) of samples. The model was trained using the training set, whereby 500 trees were constructed by randomly selecting samples through bootstrapping technique (samples are drawn with replacement). Moreover, a model randomly selected features as root node and intermediate nodes on the basis of a measure of entropy and information gain. The split at root and intermediate nodes was performed using binning and also information gain techniques implemented in the scikit-learn library (Pedregosa et al., 2011).

Total information entropy (Shannon, 1948) associated with a discrete random variable *X* which can take a finite number of unique data values x_i with corresponding probabilities $P(x_i)$ can be written as:

$$E(X) = -\sum_{i=1}^{M} P(x_i)\log_2 P x_i \qquad (5)$$

As our target variable is categorical and has repeating x_i, the formula

can be modified slightly to calculate the entropy of a target variable $E(T)$ and the probability $P(x_i)$ as below:

$$E(T) = -\sum_{i=1}^{M} \frac{f_i}{N} \log_2\left(\frac{f_i}{N}\right) \qquad (6)$$

where, f_i is the frequency of occurrence of x_i (target value labels) and *N* is the sample size of a training dataset. The $\frac{f_i}{N}$ approximates the probability $P(x_i)$ associated with the frequency of x_i.

To calculate information entropy of the target variable given a predictor/feature *F* of a numerical data type, an entropy-based binning/discretisation (e.g. ≤ 10 and $> 10°$ for slope predictor) was performed on *F* which divided the dataset into two branches/groups. The model chose the bin which produced a maximum information gain. The expression for the target's entropy given a predictor can be written as:

$$E(T, F) = \sum_{v \in F}^{M} \frac{f_v}{N} E(F) \qquad (7)$$

where, f_v is the frequency of occurrence of a predictor value given a target label (Yes/No) and a bin, and $E(F)$ is the entropy which is calculated as equation (6) for a frequency of occurrence of a predictor. The information gain was calculated as the difference of $E(T)$ and $E(T,F)$:

$$I(G) = E(T) - E(T,F) \qquad (8)$$

A predictor which produced a maximum information gain was used as the root node and others as intermediate nodes. A branch with zero entropy was the leaf/terminal node (predicted class) with homogenous data and class labels. A branch with entropy greater than zero was subjected to further splitting recursively (repeat all processes) until a leaf node was pure. The class label was based on a majority of votes received by the trees whose votes were weighted by their probability estimates.

The performance of the model was evaluated against the test dataset. The model was run up to 1000 iterations over the test dataset with samples drawn with replacement every iteration and then the confidence interval of the model accuracy was calculated. The classification accuracy of the model at 95% confidence interval was calculated to be between 94.2% and 96.9% (Fig. S2). Therefore, the model was deployed to predict class labels for new datasets collected from the eight test sites. For making class predictions on new datasets (L-0 DOIs not used for training the RFCM) using the trained model, the steps 1, 2, 3, and 4 (Fig. 3) except class labelling in step 4 were repeated. Based on a predicted class label, objects with class label "1" were retained as glacial lakes while objects with label "0" were discarded as non-glacial lake objects. All these steps for mapping glacial lakes were implemented automatically using python package "GLakeMap" that we have developed. It is mainly based on scikit-learn (Pedregosa et al., 2011), snappy (Peters, 2020), and arcpy (Esri, 2020) python libraries.

3.5. Definition, accuracy, and uncertainty of glacial lake mapping

We defined glacial lakes as those water bodies which are located within a 7 km radius of a glacier outline obtained from the GLIMS database (Raup et al., 2007; GLIMS, 2020). The 7-km threshold mostly complies with the existing definitions such as with respect to elevation, geolocation, and hydrology. It was also an adequate threshold distance for mapping even subsidiary glacial lakes associated with a fully grown glacier-contact lakes. For instance, a subsidiary glacial lake associated with a large ice-contact glacial lake is located beyond 5 km from a glacier terminus or the nearest glacier boundary (e.g. see location 28°31′35.5″N 58°38′11.4″E). The global availability of glacier outlines allowed us to fully automate the workflow for mapping glacial lakes, while it still abided the various definitions of glacial lakes. Following the existing studies (Ukita et al., 2011; Zhang et al., 2015), we included glacial lakes with a size greater than or equal to 0.01 km^2. This size is adequate to be

1) correctly identified and mapped by the current resolution of satellites, and 2) glacial lakes are perennial and large enough to be considered for hazard assessment unlike supra-glacial ponds which are smaller than this size threshold and are ephemeral (Miles et al., 2017b).

The accuracy of glacial lake mapping was assessed against the number of type-II DOIs predicted by the RFCM on new datasets and by counting how many of type-II DOIs are glacial lake and non-glacial lake objects. Thus, the accuracy of glacial lake mapping was assessed at various levels. Broadly, it can be classified into two main categories: 1) the ability of the method to detect/classify glacial lakes correctly; 2) the ability of the method to delineate glacial lake surface and shoreline boundary accurately. The former was further divided into three types: true positive (TP), false positive (FP) and false negative (FN). The latter was also categorized into four categories based on the lake area and shoreline accuracy (Table 1). Both accuracies were combined to decide whether manual intervention (manual improvement of lake surface area and outline) is necessary.

In addition, the glacial lake detection accuracy was assessed visually by overlaying detected and classified type-II DOIs over the TCC image generated using stacked Red, Green, Blue (RGB) channels of S-2 MSI image acquired over the Koshi basin and Bhutan Himalaya. The number of TP, FP, FN polygons were catalogued to calculate detection accuracy. The detection accuracy was assessed over three test sites (Boshula mountain range, Bhutan Himalaya, and Koshi basin) against the manually digitised glacial lake inventory dataset available for the entire HMA (Zhang et al., 2015). These sites were chosen due to a high density of glacial lake distribution per glacier area (Fig. 2). The accuracy of glacial lake area and outline of an automated approach was assessed quantitatively by comparing to a manually digitised glacial lake area and outline as follows: a total of 80 samples (including also the frozen glacial lakes) were digitised using TCC image as a reference obtained over the Bhutan Himalaya and the Koshi basin. Different sizes, state, and turbidity were included in the samples to capture different characteristics of glacial lakes. An absolute and relative difference between glacial lake areas was calculated using the following formula:

$$D_{rel} = \frac{|x - y|}{\left(\frac{|x+y|}{2}\right)} = \frac{|\Delta|}{f(x, y)} \tag{9}$$

where D_{rel} is the relative difference, $|\Delta|$ is the absolute difference, x and y are lake areas obtained from automated and manual methods respectively. The absolute difference was scaled by the function of the absolute value of their arithmetic mean $f(x,y)$ as a reference value. Defining relative difference is difficult because there is no actual reference value from a field survey to scale the absolute difference. Furthermore, a simple

Table 1
Glacial lake mapping (detection and delineation) accuracy score table. For detection accuracy: True Positive (++ +), False Positive and False Negative (−); for outline delineation accuracy: complete (++ +), partial (++), little (+), fail (−).

Glacial lake mapping accuracy	Detection accuracy	Delineation accuracy	Remarks	Manual Intervention required?
Complete (++ +)	+ + +	+ + +	Accurately detected and delineated	No
Partial (++)	+ + +	++	Accurately detected, but satisfactorily delineated	Yes
Little (+)	+ + +	+	Accurately detected, but satisfactorily delineated	Yes
Fail (−)	−	−	Not detected and delineated	Yes

linear regression model (ordinary least squares regression) was fitted to model the relationship between the dependent variable y (lake areas from manual technique) and independent variable x (lake areas from the automated method).

The mapping accuracy of glacial lakes was also determined by the shoreline position. The uncertainty in the shoreline position ($e_{outline}$) was determined as the root sum squares of half the resolution of multi-source data (x_i), in addition to their co-registration error (e_{coreg}).

$$e_{outline} = \sqrt{\sum_{i=1}^{n} (x_i)2} + e_{coreg} \tag{10}$$

Given the resolution of S-1 SAR and S-2 MSI data (10 m and 20 m) and the co-registration error of 20 m, a glacial lake shoreline position can be measured with an accuracy of ±31.18 m when both datasets are used. The co-registration error of 20 m was determined by computing a linear distance between manual and automated shoreline positions. Moreover, the outlines of Chubda Tsho (located in the north-eastern Bhutan Himalaya) from both methods were compared and validated against the outline of the same but obtained using the Global Navigation Satellite System (GNSS) measurement from 18 October 2018. A summation of co-registration error with resolution errors, when both datasets are used, is important because decision-rules evaluate images pixel by pixel by exploiting inter-pixel spatial relationship. The uncertainty of glacial lake area (e_{area}) can be defined as a function of uncertainty of outline and perimeter (l) of a glacial lake outline as follows:

$$e_{area} = \sqrt{\left(e_{outline}\right)^2} \, l \tag{11}$$

As a result, the uncertainty of lake area depends on the accuracy of glacial lakes outline position and size.

4. Results

4.1. L-0 discrete objects of interest (DOIs) and its segmentation from satellite images

The results of rule-based segmentation of S-1 SAR and S-2 MSI images are L-0 DOIs which have reflectance and radar backscatter strengths similar to glacial lakes. The L-0 DOIs stemmed from the areas with low radar backscatter and low spectral reflectance such as radar and mountain shadows. However, a majority of them (70–85% across the test sites) originated from using S-1 SAR data alone in R4. The common characteristics of L-0 DOIs across the test sites were varying degrees of spectral reflectance/turbidity in S-2 MSI images. A qualitative assessment of the FCC image of S-2 MSI acquired on 22 November 2017 over the eastern Koshi basin indicated that it contains many L-0 DOIs which differ in sizes, shadow depth, and turbidity (Fig. 4(a) and (f)). A classification of L-0 DOIs indicated that the type-I DOIs were mainly characterized by low average NDWI$_{blue}$ (−0.08), NDWI$_{green}$ (−0.11), compactness ratio (0.18), and high slope values (36.99°) (Table S2).

The type-II DOIs with frozen surface were more common in the Himalayas compared to northern Tien Shan, Swiss Alps, and Peruvian Andes, although the presence of ice in the satellite images might depend on the time of the year of the image acquisition and their suitability for glacial lake mapping. Some type-II DOIs were frozen and some contained icebergs from a calving glacier (Fig. 4(f)). Similarly, type-II DOIs with frozen surfaces, varying degrees of turbidity, and with mountain shadows were observed in the S-2 MSI TCC image acquired over the Bhutan Himalaya on 22 September 2017 (Fig. S3). An integrated use of the NDWI images (calculated using blue, green, and NIR bands) and S-1 SAR radar backscatter images successfully addressed glacial lake mapping challenges (Fig. 4 and Fig. S3). For example, the use of the NDWI (NDWI$_{blue}$, NDWI$_{green}$) enhanced the presence of low-turbidity type-II DOIs and suppressed vegetation and ice features in the NDWI maps. However, they poorly enhanced the presence of highly turbid and frozen type-II DOIs
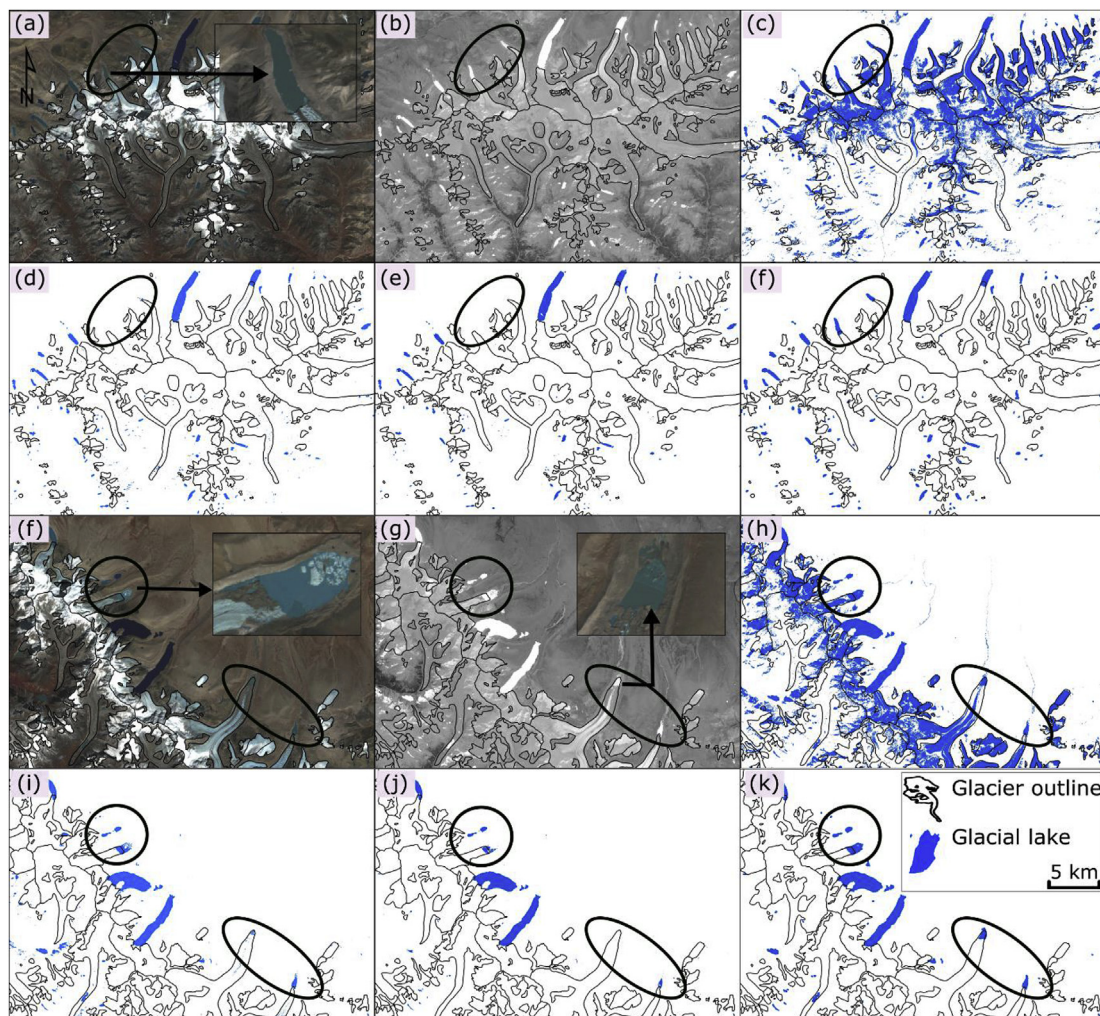
Fig. 4. Examples of image segmentation using global thresholds and rules. (a) and (f) are S-2 MSI false colour composite (RGB – Bands 8-4-3) image acquired over the Koshi basin on 22 September 2017. A subset of images is shown to represent a glacial lake with high-turbidity (a) and frozen surface with floating icebergs (f & g). (b) and (g) are the corresponding NDWI$_{green}$ images with the enhanced glacial lakes features in the map. (c) and (h) are the results of image segmentation with a global threshold of 0.05 for NDWI$_{green}$ map. Similarly, (d) and (i) are the results of using 0.3; (e) and (j) using 0.6. (f) and (k) are the results of using multi-source, rule-based image segmentation and a random forest classifier model. The top half of the image is from the eastern Koshi basin and the bottom half is from the western Koshi basin (see Shrestha et al. (2017) for the basin description). (For interpretation of the references to colour in this figure legend, the reader is referred to the Web version of this article.)

(Fig. 4(b) and (g)). On the other hand, the extent of the frozen type-II DOIs was accurately represented by S-1 SAR backscatter images and appeared as dark, non-frozen type-II DOIs (Fig. S3(a) and (d)).

The use of a global threshold such as 0.05 to segment the NDWI images for L-0 DOIs showed that the majority of glacier surfaces were segmented instead and vegetated surfaces were eliminated (Fig. 4(c) and (h)). Furthermore, it was evident that the use of 0.05 alone as global threshold was not suitable as 1) boundary between the L-0 DOIs and surrounding glacier or land was not defined at all; 2) the commission error was high as it mapped a majority of glacier surface. On the other hand, the use of 0.3 and 0.5 thresholds on NDWI maps produced better results, as the boundary between L-0 DOIs and land/glacier was mostly clear (Fig. 4(d), (e), (i) and (j)). A use of higher global NDWI threshold successfully eliminated land, vegetation, and glacier surface, but at the same time it also eliminated some high-turbidity and frozen L-0 DOIs (Fig. 4(d) and (e)).

For the extraction of those frozen L-0 DOIs, the use of the NDWI$_{green}$ threshold 0.3 was partially suitable (Fig. 4(i)) but not 0.5 (Fig. 4(j)). As a result, an omission error was greater when higher global thresholds were used. Nevertheless, when these thresholds and the NDWI maps were combined with S-1 SAR backscatter image with its own threshold and in

the form of rules, it can be seen that the L-0 DOIs, including highly turbid and frozen L-0 DOIs, were successfully detected and delineated (Fig. 4(f) and (k); Fig. S3). The thresholds, NDWI maps, and radar backscatter maps were thus highly complementary while segmenting L-0 DOIs.

4.2. Predicting class label for L-0 DOIs using the RFCM and their distribution

As the rule-based multi-source image segmentation technique generated L-0 DOIs (Table 2) through satisfying one of the rules that were defined in subsection 3.3, they must be further mapped into either as type-I DOIs (with class label "0"/non-glacial lake objects) or type-II DOIs (with class label "1"/glacial lake objects). The mapping of L-0 DOIs into their respective types was achieved by using the RFCM. The RFCM was able to robustly learn mathematical relationship between the six predictors and the target variable (glacial lake/non-glacial lake DOIs) to make prediction on the new unseen L-0 DOIs. The highest number of non-glacial lake objects were seen in the western Himalaya, central Pamir, and south-eastern Tibetan Plateau. The highest number of glacial lakes were observed in the eastern Himalaya, central Himalaya, and Peruvian Andes. However, this distribution is before the normalization by its

Table 2
Non-glacial lake objects (Type-I DOIs) and glacial lake objects (type-II DOIs) associated with the test area and the glacier size respectively after applying the rule-based multi-source image segmentation and random forest classifier model. A sum of number of type-I DOIs and type-II DOIs gives a total number of L-0 DOIs in the test area following rule-based multi-source image segmentation.

Sl.no	Test sites	Mapping area (km^2)	Glacier area (km^2)	Non-glacial lake objects (No.)	Glacial lake objects (No./%)
1	South-eastern Tibetan Plateau (TP)	58,591	5705	71706	846/1.17
2	Eastern Himalaya (EH)	29,410	1506	15255	784/4.89
3	Central Himalaya (CH)	34,035	3206	12976	476/3.54
4	Western Himalaya (WH)	54,133	6526	64307	310/0.49
5	Central Pamir (CP)	60,280	8590	59833	211/0.35
6	Northern Tien Shan (TS)	23,015	771	8619	107/1.23
7	Swiss Alps (SA)	38,279	1695	19273	239/1.22
8	Peruvian Andes (PA)	29,474	587	8352	284/3.29

respective test and glacier size.

The distribution of non-glacial lake objects per 500 km^2 of test site was highest in the south-eastern Tibetan Plateau (612), western Himalaya (594) and central Pamir (496). The lowest number was observed in the northern Tien Shan (187) and Peruvian Andes (142). The number of glacial lakes per 500 km^2 of glacier size was highest in the eastern Himalaya (250) and Peruvian Andes (242). The lowest number was observed in the western Himalaya (23) and central Pamir (12) (Fig. 5).

From the above results, it is clear that the majority of L-0 DOIs are non-glacial lake objects. In every test site only the small proportion of L-0 DOIs, the lowest of 0.35% in the central Pamir and the highest of 4.89% in the eastern Himalaya, represents glacial lakes. Nevertheless, the RFCM correctly predicted their class labels irrespective of their imbalanced distribution.

4.3. Glacial lake mapping accuracy

4.3.1. Detection and delineation accuracy

The mapping accuracy of the method is based on its ability to accurately segment and classify glacial lakes. The detection accuracy of the method ranged between 94.79% (central Pamir) and 99.47% (eastern Himalaya). The delineation accuracy of the method was between 97.07% (northern Tien Shan) and 98.94% (south-eastern Tibetan Plateau). The overall delineation accuracy (98.04%) was slightly higher than the detection accuracy (97.87%). The overall mapping accuracy is partially higher in the eastern Himalaya, however, the accuracy was comparable across the test sites. The average mapping accuracy of the method was around 97.96%.

4.3.2. Accuracy of surface area and outlines

There is statistically significant (P < 0.0001) linear relationship and a strong positive correlation (R^2 = 0.99) between glacial lakes areas (N = 80 samples) derived from the manual and automated methods (Fig. S4). Furthermore, simple boxplot and histogram plots also show a similar distribution and shape of glacial lake areas between the two techniques. The absolute difference in the median values of glacial lake areas between the two techniques is very small (Fig. S4(c)).

The common observation between the datasets over the three test sites south-eastern Tibetan Plateau, eastern Himalaya, and central Himalaya is that the detection frequency of small glacial lakes (areas (x): $0.01 \le x \le 0.05$ km^2) is much higher than the size of glacial lakes greater than 0.1 km^2 except for the south-eastern Tibetan Plateau (Fig. 6). However, the peak of the frequency distribution is much higher for the automated glacial lake datasets. The overall shape of the histogram is skewed right, across all the three validation sites, for datasets derived from the automated method. The same skewness is also observed amongst manual datasets. The descriptive statistical values (minimum, first quartile, median, third quartile, and maximum) between the datasets are quite different from each other in all the three sites. The delineation of glacial lake outlines is mostly accurate for those glacial lakes which have a contrasting edge between land and water surface in a greyscale image (SAR/NDWI image). The highest and absolute horizontal positional difference in the outline was around 20 m between the GNSS measurement made in the field (18 October 2018) and automatically generated outline over Chubda Tsho in Bhutan (Fig. 7). The automated outline is highly accurate at positions 2 and 3 (<10 m difference, Fig. 7). These regions of the shoreline are easily accessible on foot with the GNSS receiver.

4.4. Characteristics of glacial lakes in different study regions

The mean area of glacial lakes is higher in the Swiss Alps (0.21 km^2), central Pamir (0.19 km^2), and central Himalaya (0.15 km^2) followed by eastern Himalaya (0.12 km^2), south-eastern Tibetan Plateau (0.11 km^2), and Peruvian Andes (0.10 km^2). Glacial lakes in the central Pamir are in general small, the relatively large mean area is due to few bigger lakes. The highest density of glacial lakes was also observed in the same areas as above. The eastern Himalaya and Peruvian Andes showed highest density of glacial lakes. The low density of glacial lakes in the central Pamir further indicated that the high mean area of glacial lakes in the region was due to the contribution of a few large lakes. A low density of glacial lakes was observed in the western Himalaya and central Pamir, where glacier mass loss is known to be small for the latter (Wester et al., 2019). The highest average elevation of glacial lakes was observed in the central Himalaya (5107 m) followed by central Pamir, eastern Himalaya, and south-eastern Tibetan Plateau (Table 4). The lowest average elevation was observed for glacial lakes in the Swiss Alps (2278 m) and northern Tien Shan (3459 m).

5. Discussion

5.1. Mapping of small glacial lakes ($0.01 \le x \le 0.05$ km^2)

In the context of glacial lake hazard assessment, accurate mapping of glacial lakes is the first and one of the most important steps amongst many chains of processes (Allen et al., 2019). However, mapping of glacial lakes remains unequivocally challenging in alpine regions, particularly due to their typically small size. Semi-automated mapping of glacial lakes, in general, is laborious during post-processing and prone to errors (commission and omission) as spectral reflectance in mountains are diverse. Consequently, they are easy to be missed and misidentified during glacial lake inventory. The manual technique is the most accurate if applied carefully by an expert using suitable datasets, but it is time-consuming when applied over a large study area (e.g. Zhang et al., 2015).

The automatic approach proposed in this study robustly overcomes the mapping challenges of small size glacial lakes as indicated by the high frequency of small glacial lakes <0.05 km^2 being detected compared to the manually mapped glacial lake datasets (Zhang et al., 2015). This is because the method can detect and delineate glacial lakes sizes as small as 0.01 km^2 automatically without having to manually identify and remove non-water objects of similar sizes or others. A huge discrepancy in the detection frequency of small glacial lakes (Fig. 6) between the
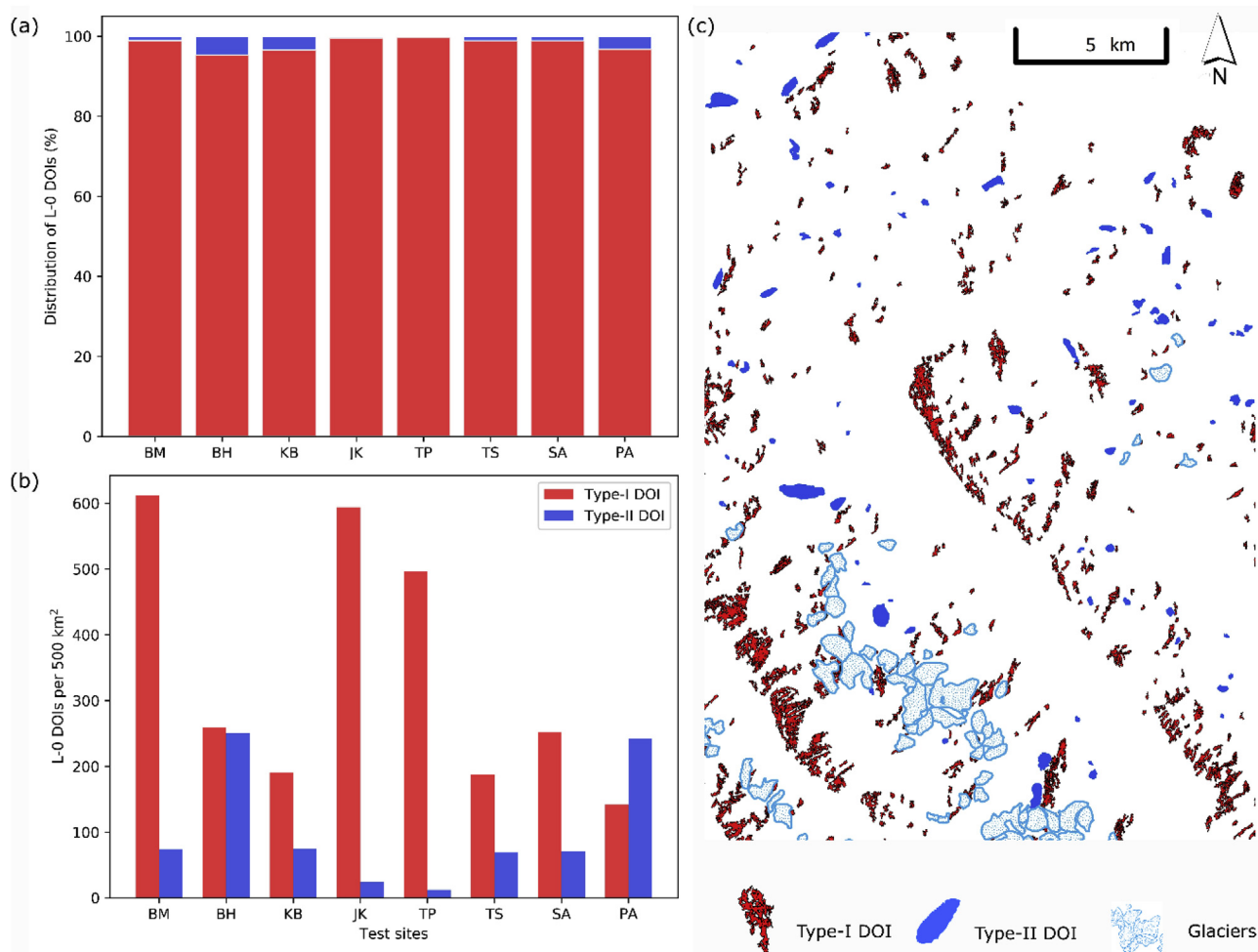
Fig. 5. The percentage distribution of type-I (red bars and patches) and –II DOIs (blue bars and patches) across the test sites (a). The distribution of type-I and –II DOIs per 500 km² test area (refer Table 2 for their sizes). The pictorial representation of type-I and –II DOIs along with the glaciated area (c). Refer Table 2 for the abbreviations for the test sites in Figure (a) and (b) x-axis. The glacier outlines are taken from the GLIMS website. (For interpretation of the references to colour in this figure legend, the reader is referred to the Web version of this article.)

validation dataset (Zhang et al., 2015) and our method could be due to the difference in definition of glacial lakes considered, datasets used, and the year of images acquired for glacial lake mapping. For instance, Zhang et al. (2015) have used Landsat data (30 m resolution) from 2010 and considered the threshold distance of 10 km from glacier outlines. On the other hand, our results suggest that the integration of the rule-based image segmentation technique on multi-source data and the random forest classifier firmly accomplished automatic detection and delineation of glacial lakes with high accuracy. A prior segmentation of satellite images into L-0 DOIs using rules ensured that the location information is preserved and the classification of images into different land cover classes unnecessary. The method can extract glacial lakes from satellite images systematically following the defined rules.

Each rule detects and delineates glacial lakes using one or a combination of rules and datasets. Each rule has its level of strength. For instance, R1 has the potential to extract very low- and low-turbidity glacial lakes. It has been implemented in the Swiss Alps (e.g. Huggel et al., 2002) and the central Himalaya (Bolch et al., 2008; Shrestha et al., 2017) to map glacial lakes. The rules R2 and R3 were designed keeping in mind the challenges to map medium- and high-turbidity glacial lakes using optical datasets. Here, an inter-pixel spatial relationship between the two entirely different sources of datasets (optical and active) is explored to extract glacial lakes. Rule R4, which uses only SAR data, was designed to extract glacial lakes when the optical datasets are under cloud cover. This rule was successfully implemented in the Bhutan

Himalaya for detecting glacial lakes (Wangchuk et al., 2019).

5.2. Methodological advancements

Our method (combination of multi-source image segmentation and a RFCM) has three main strengths: 1) the strength of the multi-source image segmentation technique is its ability to nest a rule within rules and combine their results into glacial lake objects. Although the rule-based image segmentation technique extracted all most all glacial lake objects, a majority of them were type-I DOIs stemmed from mainly shadowed areas that also satisfied one of the rules. Therefore, they must be first identified and second removed either manually, semi-automatically or automatically. The previous studies have used manual and semi-automatic techniques. The semi-automatic removal of type-I DOIs requires terrain information which is usually derived from DEMs (Huggel et al., 2002; Bolch et al., 2011); 2) we used the RFCM to predict their class labels and remove them automatically based on the predicted class labels.

The prediction of the class labels was based on six feature datasets, including the terrain information, from which the model learned certain function that mapped L-0 DOIs into one of the classes. The L-0 DOIs with predicted label "0" were non-glacial lake objects (type-I DOIs), while L-0 DOIs with predicted label "1" were glacial lake objects (type-II DOIs). The former was eliminated automatically during the post-processing by identifying those L-0 DOIs with the label "0". Therefore, an ability of the
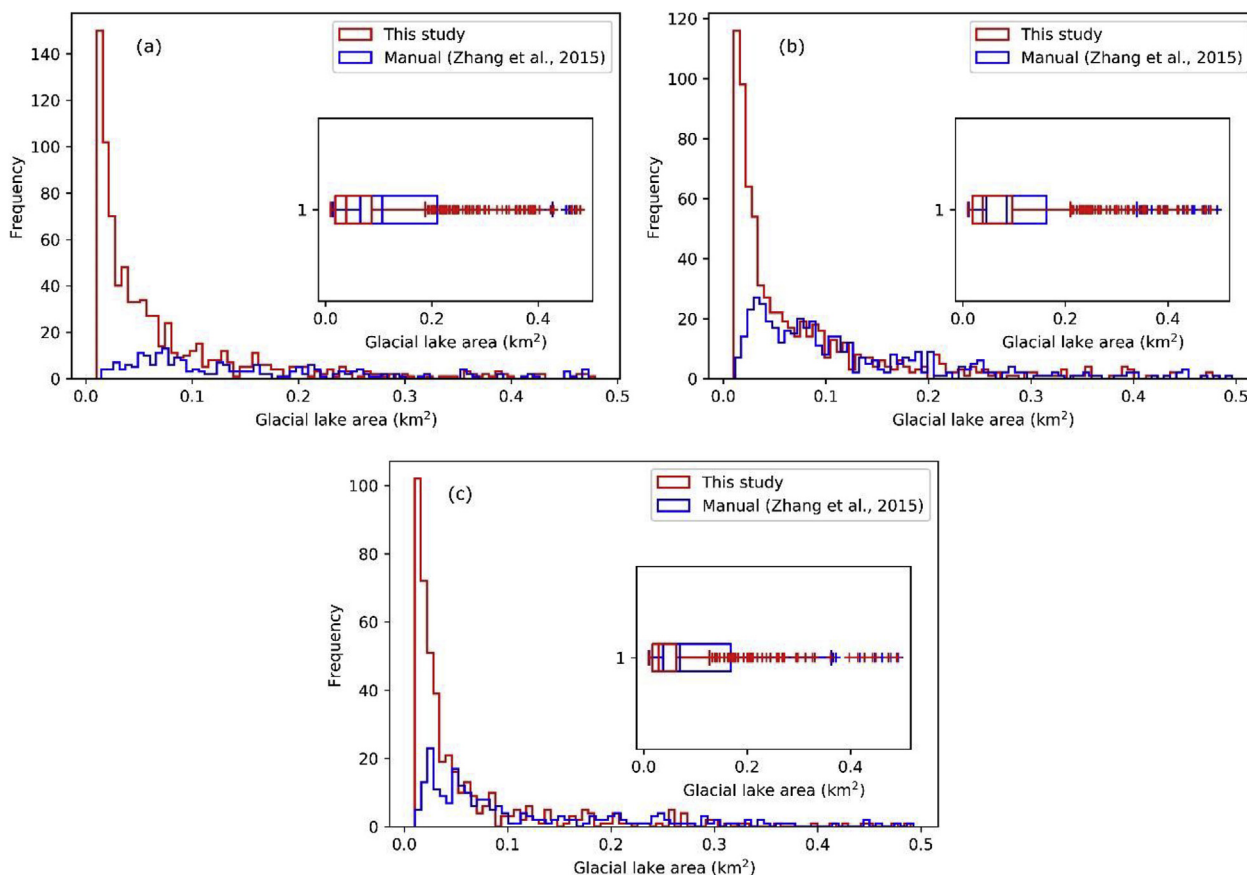
Fig. 6. Comparison of glacial lake detection capability between the manual and our automated method. The automated method is highly robust for mapping small glacial lakes as indicated by the high frequency of small glacial lakes (e.g. 0.05 km^2) detection: south-eastern Tibetan Plateau (a); eastern Himalaya (b); central Himalaya (c).
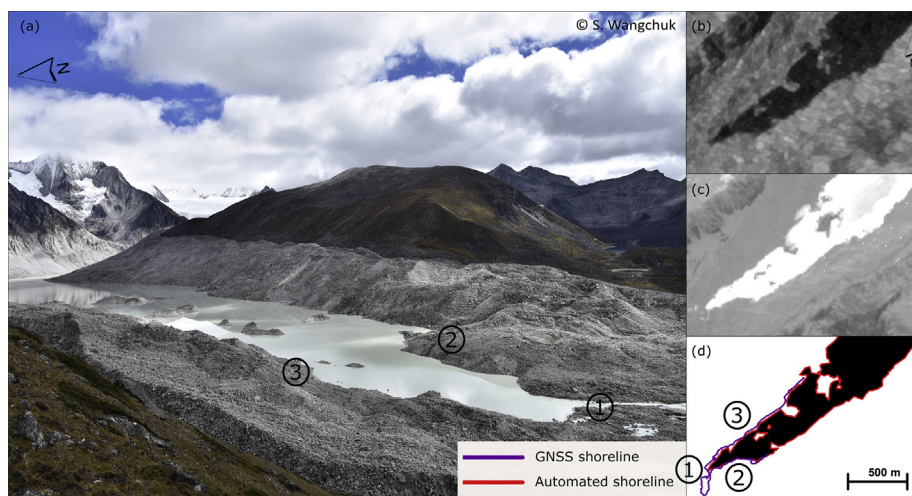
Fig. 7. (a) Chubda Tsho on 18 October 2018 (Photo: S. Wangchuk), (b) S-1 SAR image (acquired on 2 November 2017) of the same area, (c) The NDWI map of S-2 MSI image (acquired on 6 November 2017). (d) Comparison of the automated outline with GNSS outline.

RFCM to predict class labels for L-0 DOIs automatically makes the method robust and superior compared to the manual and semi-automated techniques; 3) the rule-based image segmentation technique and RFCM combined is almost independent of satellite scene selection for glacial lakes mapping, although we recommend satellite scene selection to maintain better performance. The contrast between the glacial lake surface and the land is higher when images are free from seasonal snow and ice (Wangchuk et al., 2019).

5.3. Accuracy of mapping glacial lakes

High accuracy of glacial lake detection and delineation accuracy (both above 95%) achieved by our method (Table 3) is due to its ability to correctly extract glacial lake objects from satellite images using rule-based image segmentation technique and predict their correct class labels by the RFCM (Figs. 5 and 6). In mountain regions, a presence of cast shadows in satellite images is de facto unavoidable. Such features in

Table 3
Number of glacial lakes and water bodies (e.g. rivers) detected. Number of glacial lakes that requires outline adjustment (OA) and manual intervention (MI). Detection accuracy (DetA), delineation accuracy (DelA), and mapping accuracy (MA) of glacial lakes. Refer Table 2 for abbreviations in test sites column.

Sl. no	Test sites	Glacial lakes (No.)	Water Bodies (No.)	False Positive (No.)	False Negative (No.)	OA	MI	DetA(%)	DelA(%)	MA(%)
1	TP	846	108	9	5	4	126	98.35	98.94	98.64
2	EH	754	4	1	3	7	15	99.47	98.67	99.07
3	CH	476	0	3	4	5	12	98.53	98.11	98.32
4	WH	310	17	3	3	3	26	98.06	98.06	98.06
5	CP	211	68	8	3	2	81	94.79	97.63	96.21
6	TS	107	3	0	2	1	6	98.13	97.20	97.66
7	SA	239	39	5	2	4	50	97.07	97.49	97.28
8	PA	284	20	0	4	1	25	98.59	98.24	98.42

Table 4
Attributes of glacial lakes across the test sites. Refer Table 2 for the glacier size.

Sl.No	Test sites	Mean area (km^2)	Density (per sq.km glacier)	Mean elevation (m.a.s.l)
1	TP	0.11	0.15	4615
2	EH	0.12	0.5	4822
3	CH	0.15	0.15	5106
4	WH	0.07	0.05	4475
5	CP	0.19	0.02	4985
6	TS	0.06	0.14	3459
7	SA	0.21	0.14	2278
8	PA	0.1	0.48	4472

satellite images influence accurate mapping of glacial lakes. In conventional methods, because of the use of the semi-automated techniques such as the NDWI maps and global thresholds without any other complementary datasets, the footprints of cast shadows are mapped along with the glacial lakes thus making post-processing time-consuming. In contrast, our proposed method automatically extracts glacial lakes using rules and the RFCM and non-glacial lake objects such as land/glacier are eliminated. Moreover, when footprints of cast shadows partially cover glacial lakes, the rules can correctly identify and delineate those glacial lakes based on the inter-pixel relationship between satellite images. This is indicated by the small number of glacial lakes that require outline adjustment (Table 3). To consider a subset of satellite images as glacial lakes, pixels must fully satisfy the rules to be considered as glacial lakes. This is achieved by searching pixels in the image using *if − then* rules and establishing inter-pixel relationships. Therefore, the proposed method is highly optimized to output glacial lakes with minimum false positive (Table 3).

Another advantage of the method stems from its ability to map high- and very high-turbidity glacial lakes, which is one of the major challenges encountered by the conventional methods (Huggel et al., 2002; Bolch et al., 2008). Turbidity varies from lakes to lakes and even within a lake. A use of high NDWI thresholds such as 0.4 (Fig. 4 (d) and (i)), and 0.6 (Fig. 4 (e) and (j)) omits many high turbidity glacial lakes, while the use of low NDWI thresholds such as 0.05 (Fig. 4 (c) and (h)) commits many non-water features as glacial lake objects. Our method overcomes these challenges by giving a user the flexibility to input a wide range of the NDWI threshold values greater than or equal to 0.05. In this method, we used 0.05 (aimed at mapping high-turbidity glacial lakes), 0.3 (aimed at mapping medium-turbidity glacial lakes), and 0.6 (aimed at mapping low-turbidity glacial lakes) in the form of rules. As a result, our method ensures extraction of glacial lakes irrespective of their turbidity and with minimum commission and omission errors. This is achieved by also using SAR backscatter images of glacial lakes as one of the complementary input datasets. According to Wangchuk et al. (2019), a backscatter intensity threshold of less than −14 dB is adequate for mapping glacial lakes in the Himalayas. Hence, S-1 and S-2 images are highly complementary making selection of thresholds less sensitive to changes in glacial lake characteristics and satellite scenes.

Seasonal snows and frozen glacial lakes are known for their

interference in glacial lake mapping techniques. Seasonal snows alter reflectance of land surface and glacial lake vicinity resemble a glacial lake. Sometimes, they accumulate on a partially frozen glacial lake surface and alter its reflectance. Our method can adequately identify glacial lakes with frozen water surface as long as they satisfy thresholds defined in the rule-based segmentation to be considered as glacial lakes and its correct prediction of class label by the RFCM. The method was found to be robust when glacial lake surface was uniformly frozen and the shoreline was clearly defined. Here the main advantage of the method stems from using SAR data. Glacial lakes with partially and uniformly frozen surface still appeared dark in SAR backscatter data due to the specular reflection of radar pulses by the smooth frozen water surface (Wangchuk et al., 2019; Strozzi et al., 2012).

5.4. Limitations

Having mentioned all the improvements there are also certain caveats in our method. The first is minimum thresholds that have to be defined for radar backscatter and NDWI maps to extract L-0 DOIs. We used 0.05 for NDWI$_{green}$ and −14 dB for SAR data. Although these thresholds were found less sensitive and smaller by many orders of magnitude compared to conventional methods, below these thresholds, for instance a use of 0.03 for NDWI$_{green}$, few glacial lakes (in the range of 2–7) started to lose their true shoreline position to land or a glacier as indicated by the number of glacial lakes that required outline adjustment. Consequently, the outline was jagged and corresponding CR value of a glacial lake was low. While making predictions using the RFCM, the likelihood of considering them as type-I DOIs is high as glacial lakes were trained to take slightly higher values of CR. Similar considerations apply to, for instance, those glacial lakes which have high average slope values within the zone because of inaccurate DEM values on the water surface (Fig. S5). On the other hand, it would also depend on the properties of other feature datasets used for training the RFCM. For instance, glacial lakes with high NDWI values, low radar backscatter, low slopes, but low CR has a higher likelihood to be classified as glacial lakes. Similarly, glacial lakes with high slope values but low NDWI, low radar backscatter, and high CR values could correctly be classified as glacial lake (Fig. S6). Given all these possibilities, it is evident from our result that the feature datasets we have chosen and thresholds we used were highly adequate for mapping glacial lakes across alpine regions irrespective of their state and turbidity. An accurate result could also be attributed to ensemble learning of the RFCM as trees vote to predict the final class label of L-0 DOIs.

False positive glacial lakes were mainly found on a glacier surface (commission error). The reason is straightforward because some L-0 DOIs had all the attributes of a glacial lake. They had higher compactness ratio, low slope, and low radar backscatter or high NDWIs values. Such areas were, mostly cast shadows from mountains on the low gradient glacier surface. However, the commission error is negligible when compared to the conventional methods which use single NDWI threshold and shadow mask (Rounce et al., 2017; Huggel et al., 2002). For instance, only nine were false positive amongst 800 glacial lakes mapped over 50,000 km^2 in

the south-eastern Tibetan Plateau, where the image tiles were severely covered by seasonal snows and the DEM is of poor quality on the water surface (Allen et al., 2019).

Delineation of glacial lake outlines is slightly challenging for few glacial lakes 1) when the spatial contrast between the lake surface and shadow is not clear, and 2) when the inter-pixel spatial relationship extends beyond a shoreline position. The former drawback was observed for glacial lakes delineated with a single rule (e.g. rule one and four), while the latter was observed for rules linked by AND operation (object intersection). Nevertheless, the number of glacial lakes that require outline adjustment is less than 1.67% across all the test sites (Table 3). The outline delineation is robust for those glacial lakes which have distinct spatial contrast with surrounding areas such as land or glacier.

Finally, a low number of glacial lakes were not detected (omission error) by the rule-based image segmentation technique. Since the results of the rule-based image segmentation technique (L0 DOIs) are used as zones for extracting new predictor datasets for the RFCM, the error is propagated into results. In other words, those glacial lakes which are not detected by the former method are not the part of observations for the latter. Such failure in the detection of glacial lakes was found in the areas where glacial lakes were entirely obscured by the layover in SAR backscatter images and the NDWI values were less than 0.6 (Fig. S7). In such areas, the radar backscatter is bit high as the position of the ground is reversed in the SAR image accompanied by a low incidence angle between a radar beam and its intercepting surface.

5.5. Comparison with existing methods and inventories

The proposed method was built upon the exiting studies and knowledge gained through a decade of research. The most used technique in our test sites is surprisingly still manual editing of lakes followed by the NDWI maps-based thresholds (Table S3), initially proposed by Huggel et al. (2002) for the glacial lakes in the Swiss Alps and are widely transferred across the Himalayas and the Andes. The manual delineation of outlines is accurate but is not trivial to reproduce even delineated by a same individual. The semi-automated techniques enjoy partial reproducibility, however, involve removal of misclassified lakes (e.g. cast shadows) during post-processing (Bolch et al., 2008). In some areas, the latter technique entirely fails to produce good results (e.g. Mergili et al., 2013). Therefore, both approaches are suitable only at a local scale as its implementation over a larger scale would be time-consuming. Furthermore, an inconsistent use of above approaches and datasets based on their suitability in an area have resulted in the different use of lake size thresholds, therefore, producing inconsistent lake numbers during inventory (Table S3). Under the current scenario, a comparison of glacial lake inventory results and lake evolution across alpine regions would be highly ambiguous.

Previously, the most widely used data for glacial lake mapping were Landsat data (Table S3). Since the launch of the Copernicus satellites Sentinel-1 and –2, data from these satellites are increasingly used as S-1 SAR can see through the clouds and S-2 have a higher spatial (10 m) resolution and revisit time (5 days with S-2A and -2B). Furthermore, an alternative approach to the conventional techniques (Table S3) are the evolving machine learning techniques. The use of S-2 data driven NDWI maps and the random forest classifier for mapping lakes on ice sheets have already gained momentum (e.g. Dirscherl et al., 2020; Moussavi et al., 2020). The use of S-1 SAR data for mapping glacial lakes is also proven to be robust although removal of misclassified pixels relies on optical datasets (Miles et al., 2017a; Wangchuk et al., 2019). The use of machine learning techniques coupled with S-1 SAR backscatter data and S-2 NDWI maps would further advance the methodology for alpine glacial lake mapping and inventorying. In our proposed method, we have successfully integrated random forest classifier, S-1 SAR and S-2 MSI data. The method utilizes and integrates strengths of existing methods (cf. Bolch et al., 2008; Gardelle et al., 2011; Huggel et al., 2002; Wangchuk et al., 2019) accompanied by the random forest algorithm to enhance the performance of lake mapping and inventorying. One of the key strengths also originates from the fact that the random forest is applied at object-based level (image segmentation is performed and shape factor is used) in contrast to training, testing, and predicting on a pixel-based sample collections (e.g. Dirscherl et al., 2020; Moussavi et al., 2020). The object level classification is more accurate than the latter (Robson et al., 2015).

The proposed method was found to be highly robust against all forms of disturbing and challenging factors (i.e. shadows, turbidity, and ice surface) encountered during glacial lake mapping. The glacial lake outline is consistent with the inventory results by ICIMOD (ICIMOD, 2011) and Zhang et al. (2015), compared over the Nepal Himalaya (Fig. S8). A further comparison of our lake outlines with the datasets by the National Water Authority of Peru (ANA, 2014) over the Peruvian Andes shows good alignment (Fig. S8).The method has the potential to resolve current inconsistencies in glacial lake inventory datasets across the alpine regions and paves way forward towards regionally based consistent comparison of glacial lake evolution and inventory.

6. Conclusions

Glacial lakes in alpine regions are typically located in remote locations and high elevations. In these areas, field-based mapping and monitoring of glacial lake hazards are challenging because of the remoteness of the areas, a high number of glacial lakes, and their inaccessibility. As a result, remote-sensing based approaches are highly preferred to field based mapping and monitoring approaches. In recent years, the former methods have been growing rapidly due to the free availability of data and large spatial coverage. However, remote-sensing based approaches have their own drawbacks. The limitations, in particular, include their inabilities to robustly map glacial lakes over large areas due to many disturbing factors such as the cast shadows from mountains and clouds, turbidity of glacial lakes, cloud cover, seasonal snows, and frozen glacial lake surfaces. Therefore, the existing remote sensing methods introduce high commission and omission errors in the mapping results, unless these errors are minimised manually during the post-processing stage.

In this study, we proposed a method for mapping glacial lakes (also a Python package called "GLakeMap") across alpine regions which accounts aforementioned challenges automatically. The method is composed of rule-based image segmentation and random forest classifier model (RFCM). The rule-based technique extracts level-0 discrete objects of interest (L-0 DOIs) from S-1 Synthetic Aperture Radar (SAR) and S-2 Multi-spectral Instrument (MSI) images. The RFCM then predicts whether L-0 DOIs are glacial lake or non-glacial lake objects based on the six predictor datasets on which the model was trained. The predictors are the $NDWI_{blue}$, $NDWI_{green}$, near-infrared (NIR) reflectance images, radar backscatter intensity, surface slopes, and compactness ratio. The method was tested across eight alpine regions with the areas covering between $20,000 \text{ km}^2$ and $60,000 \text{ km}^2$. The method was found to be highly robust in all the eight test sites with the mapping accuracy of between 96.21% (central Pamir) and 99.07% (eastern Himalaya) and can be used to map glacial lakes irrespective of geographic and climatic conditions and glacial lakes characteristics.

Author contributions

Sonam Wangchuk designed the study, processed and analysed the data, prepared figures, and wrote codes and draft of the manuscript. Tobias Bolch guided the study and contributed to the writing and the final form of the manuscript.

Code availability

Currently, code for the Python package (GLakeMap) is available from the authors upon request.

Declaration of competing interest

No potential conflict of interest was reported by the authors.

Appendix A. Supplementary data

Supplementary data to this article can be found online at https://doi.org/10.1016/j.srs.2020.100008.

References

Allen, S.K., Zhang, G., Wang, W., Yao, T., Bolch, T., 2019. Potentially dangerous glacial lakes across the Tibetan Plateau revealed using a large-scale automated assessment approach. Sci. Bull. 64 (7), 435–445.

ANA, 2014. Inventario de Lagunas Glaciares del Perú. *ANA*.

Belgiu, M., Drăguţ, L., 2016. Random forest in remote sensing: a review of applications and future directions. ISPRS J. Photogrammetry Remote Sens. 114, 24–31.

Bolch, T., 2007. Climate change and glacier retreat in northern tien Shan (Kazakhstan/kyrgyzstan) using remote sensing data. Global Planet. Change 56 (1–2), 1–12.

Bolch, T., Buchroithner, M.F., Peters, J., Baessler, M., Bajracharya, S., 2008. Identification of glacier motion and potentially dangerous glacial lakes in the Mt. Everest region/Nepal using spaceborne imagery. Nat. Hazards Earth Syst. Sci. 8 (6), 1329–1340.

Bolch, T., Peters, J., Yegorov, A., Pradhan, B., Buchroithner, M., Blagoveshchensky, V., 2011. Identification of potentially dangerous glacial lakes in the northern Tien Shan. Nat. Hazards 59 (3), 1691–1714.

Breiman, L., 2001. Random forests. Mach. Learn. 45 (1), 5–32.

Burrough, P.A., McDonnell, R., McDonnell, R.A., Lloyd, C.D., 1986. Principles of Geographical Information Systems. Oxford university press.

Dirscherl, M., Dietz, A.J., Kneisel, C., Kuenzer, C., 2020. Automated mapping of antarctic supraglacial lakes using a machine learning approach. Rem. Sens. 12 (7), 1203.

Ehrbar, D., Schmocker, L., Vetsch, D.F., Boes, R.M., 2018. Hydropower potential in the periglacial environment of Switzerland under climate change. Sustainability 10 (8), 2794.

Emmer, A., Klimeš, J., Mergili, M., Vilímek, V., Cochachin, A., 2016. 882 lakes of the cordillera blanca: an inventory, classification, evolution and assessment of susceptibility to outburst floods. Catena 147, 269–279.

Esri, 2020. What is ArcPy [Online]. Available: https://desktop.arcgis.com/en/arcmap/10.3/analyze/arcpy/what-is-arcpy-.html.

Gardelle, J., Arnaud, Y., Berthier, E., 2011. Contrasted evolution of glacial lakes along the Hindu Kush Himalaya mountain range between 1990 and 2009. Global Planet. Change 75 (1–2), 47–55.

Gislason, P.O., Benediktsson, J.A., Sveinsson, J.R., 2006. Random forests for land cover classification. Pattern Recogn. Lett. 27 (4), 294–300.

GLIMS, 2020. Global land ice measurements from Space: monitoring the world's changing glaciers [Online]. Available: https://www.glims.org/.

Harrison, S., Kargel, J.S., Huggel, C., Reynolds, J., Shugar, D.H., Betts, R.A., Emmer, A., Glasser, N., Haritashya, U.K., Klimes, J., et al., 2018. Climate change and the global pattern of moraine-dammed glacial lake outburst floods. Cryosphere 12 (2), 1195–1209.

Huggel, C., Kääb, A., Haeberli, W., Teysseire, P., Paul, F., 2002. Remote sensing based assessment of hazards from glacier lake outbursts: a case study in the Swiss Alps. Can. Geotech. J. 39 (2), 316–330.

ICIMOD, 2011. Glacial Lakes of Nepal 2011. *ICIMOD*.

King, O., Bhattacharya, A., Bhambri, R., Bolch, T., 2019. Glacial lakes exacerbate Himalayan glacier mass loss. Sci. Rep. 9 (1), 1–9.

Komori, J., 2008. Recent expansions of glacial lakes in the Bhutan Himalayas. Quat. Int. 184 (1), 177–186.

Li, J., Sheng, Y., 2012. An automated scheme for glacial lake dynamics mapping using Landsat imagery and digital elevation models: a case study in the Himalayas. Int. J. Rem. Sens. 33 (16), 5194–5213.

McFeeters, S.K., 1996. The use of the Normalized Difference Water Index (NDWI) in the delineation of open water features. Int. J. Rem. Sens. 17 (7), 1425–1432.

Mergili, M., Müller, J.P., Schneider, J.F., 2013. Spatio-temporal development of highmountain lakes in the headwaters of the Amu Darya river (Central Asia). Global Planet. Change 107, 13–24.

Miles, K.E., Willis, I.C., Benedek, C.L., Williamson, A.G., Tedesco, M., 2017a. Toward monitoring surface and subsurface lakes on the Greenland ice sheet using Sentinel-1 SAR and Landsat-8 OLI imagery. Front. Earth Sci. 5, 58.

Miles, E.S., Willis, I.C., Arnold, N.S., Steiner, J., Pellicciotti, F., 2017b. "Spatial, seasonal and interannual variability of supraglacial ponds in the Langtang Valley of Nepal, 1999–2013. J. Glaciol. 63 (237), 88–105.

Mool, P.K., Wangda, D., Bajracharya, S.R., Kunzang, K., Gurung, D., Joshi, S., et al., 2001. Inventory of glaciers, glacial lakes and glacial lake outburst floods. Monitoring and early warning systems in the Hindu Kush-Himalayan Region, Bhutan. Kathmandu. Int. Centre Integr. Mt. Dev. 1–254.

Moussavi, M., Pope, A., Halberstadt, A.R.W., Trusel, L.D., Cioffi, L., Abdalati, W., 2020. Antarctic supraglacial lake detection using landsat 8 and sentinel-2 imagery: towards continental generation of lake volumes. Rem. Sens. 12 (1), 134.

Pedregosa, F., Varoquaux, G., Gramfort, A., Michel, V., Thirion, B., Grisel, O., Blondel, M., Prettenhofer, P., Weiss, R., Dubourg, V., Vanderplas, J., Passos, A., Cournapeau, D., Brucher, M., Perrot, M., Duchesnay, E., 2011. Scikit-learn: machine learning in Python. J. Mach. Learn. Res. 12, 2825–2830.

Peters, M., 2020. How to use the SNAP API from Python [Online]. Avail- able: http s://senbox.atlassian.net/wiki/spaces/SNAP/pages/19300362/How+to+use+ the+ SNAP+API+from+Python.

Pörtner, H.-O., Roberts, D.C., Masson-Delmotte, V., Zhai, P., Tignor, M., Poloczanska, E., Mintenbeck, K., Alegría, A., Nicolai, M., Okem, A., Petzold, J., Rama, B., Weyer, N.M., 2019. The Ocean and Cryosphere in a Changing Climate: A Special Report of the Intergovernmental Panel on Climate Change. Ipcc.

Raup, B., Racoviteanu, A., Khalsa, S.J.S., Helm, C., Armstrong, R., Arnaud, Y., 2007. The GLIMS geospatial glacier database: a new tool for studying glacier change. Global Planet. Change 56 (1–2), 101–110.

Robson, B.A., Nuth, C., Dahl, S.O., Hölbling, D., Strozzi, T., Nielsen, P.R., 2015. Automated classification of debris-covered glaciers combining optical, sar and topographic data in an object-based environment. Rem. Sens. Environ. 170, 372–387.

Rounce, D.R., Watson, C.S., McKinney, D.C., 2017. "Identification of hazard and risk for glacial lakes in the Nepal Himalaya using satellite imagery from 2000–2015. Rem. Sens. 9 (7), 654.

Shannon, C.E., 1948. A mathematical theory of communication. Bell Syst. Tech. J. 27 (3), 379–423.

Shrestha, F., Gao, X., Khanal, N.R., Maharjan, S.B., Shrestha, R.B., Wu, L.-z., Mool, P.K., Bajracharya, S.R., 2017. Decadal glacial lake changes in the Koshi basin, central Himalaya, from 1977 to 2010, derived from Landsat satellite images. J. Mt. Sci. 14 (10), 1969–1984.

Strozzi, T., Wiesmann, A., Kääb, A., Joshi, S., Mool, P., Mergili, M., 2012. Glacial lake mapping with very high resolution satellite SAR data. Nat. Hazards Earth Syst. Sci. 12 (8).

Ukita, J., Narama, C., Tadono, T., Yamanokuchi, T., Tomiyama, N., Kawamoto, S., Abe, C., Uda, T., Yabuki, H., Fujita, K., et al., 2011. Glacial lake inventory of Bhutan using ALOS data: methods and preliminary results. Ann. Glaciol. 52 (58), 65–71.

Veh, G., Korup, O., Roessner, S., Walz, A., 2018. Detecting Himalayan glacial lake outburst floods from Landsat time series. Rem. Sens. Environ. 207, 84–97.

Wang, W., Xiang, Y., Gao, Y., Lu, A., Yao, T., 2015. Rapid expansion of glacial lakes caused by climate and glacier retreat in the Central Himalayas. Hydrol. Process. 29 (6), 859–874.

Wangchuk, S., Bolch, T., Zawadzki, J., 2019. Towards automated mapping and monitoring of potentially dangerous glacial lakes in Bhutan Himalaya using Sentinel-1 Synthetic Aperture Radar data. Int. J. Rem. Sens. 40 (12), 4642–4667.

Wessels, R.L., Kargel, J.S., Kieffer, H.H., 2002. ASTER measurement of supraglacial lakes in the Mount Everest region of the Himalaya. Ann. Glaciol. 34, 399–408.

Wester, P., Mishra, A., Mukherji, A., Shrestha, A.B., 2019. The Hindu Kush Himalaya Assessment. Cham: Springer International Publishing, Basel, Switzerland.

Wilson, R., Glasser, N.F., Reynolds, J.M., Harrison, S., Anacona, P.I., Schaefer, M., Shannon, S., 2018. Glacial lakes of the Central and Patagonian Andes. Global Planet. Change 162, 275–291.

Yao, T., Thompson, L., Yang, W., Yu, W., Gao, Y., Guo, X., Yang, X., Duan, K., Zhao, H., Xu, B., et al., 2012. Different glacier status with atmospheric circulations in Tibetan Plateau and surroundings. Nat. Clim. Change 2 (9), 663.

Zhang, G., Yao, T., Xie, H., Wang, W., Yang, W., 2015. An inventory of glacial lakes in the Third Pole region and their changes in response to global warming. Global Planet. Change 131, 148–157.